Energy Advances

ROYAL SOCIETY OF CHEMISTRY

COMMUNICATION

View Article Online
View Journal | View Issue

Cite this: *Energy Adv.*, 2024, 3, 2896

Received 24th June 2024,
Accepted 25th October 2024

DOI: 10.1039/d4ya00398e

rsc.li/energy-advances

Organometallic synthesis of a high-density Pt single atom catalyst on nickel for the alkaline hydrogen evolution reaction†

Vineesh Thazhe Veettil,‡ Manoj Shanmugasundaram‡ and David Zitoun *

Single atom platinum catalysts, characterized by isolated Pt atoms dispersed on suitable supports, exhibit high hydrogen evolution catalytic mass activity. The activity is usually limited by the low density of Pt atoms on the substrate. Herein, we report on a single step synthesis of a catalyst from organometallic precursors of Ni and Pt which yields a high density of Pt atoms on Ni nanoparticles dispersed on a carbon support. The spontaneous formation of Pt single atoms on the surface of Ni has not been reported in a single step reaction and is a unique feature of the organometallic route. This route allowed us to increase the atomic ratio of single Pt atoms to Ni up to 10% compared to 2% reported previously. Single Pt atoms on Ni catalysts display a high hydrogen evolution reaction activity of 660 mA mg_{Pt}^{-1} (8 times more than that of commercial Pt) and stability as HER catalysts compared with commercial Pt/C catalysts.

1. Introduction

The escalating global energy demands and adverse environmental impacts of traditional energy resources are threats to human health and environmental protection.[1,2] Sustainable energy calls for the development of an alternative clean, renewable and economical fuel.[3,4] Hydrogen is identified as one of the best carbon-negative renewable futuristic energy sources and a promising alternative to fossil fuels. The effective production, storage and energy conversion of hydrogen are imperative to a reliable future.[5–8] However, the majority of the hydrogen produced today is derived from steam-reformed methane, which is sourced from fossil reserves and produces a substantial amount of CO_2.[9–11]

Electrochemical water splitting is regarded as a green and sustainable route to produce hydrogen, in which the hydrogen evolution reaction (HER) is the essential step. A key aspect for scalable hydrogen production is developing HER catalysts with high efficiency and low cost.[12–15] Fitting of theoretically calculated exchange-current densities against the hydrogen adsorption free energy (ΔG_H) shows a "volcano plot" over different metals, among which platinum was regarded as the best pH universal HER catalyst. Platinum is very close to the maximum of the volcano plot, with almost a thermo-neutral ΔG_H value.[16,17] However, the high cost and low abundance hamper the practical application of Pt HER catalysts. Developing highly active and Pt-free catalysts with earth-abundant elements (*e.g.*, Co, Ni, and Fe) is another approach to reduce the cost of HER catalysts.[18–23] Although much progress has been made to develop Pt-free catalysts, their HER performance still requires improvement.

To overcome these limitations, downsizing the Pt NPs into Pt single atoms is used to maximize the metal utilization for cost-effective HER catalysts. Reducing the size of the Pt NPs to single atoms could significantly decrease the noble metal usage and increase their catalytic activity, which is highly desirable to enhance the Pt utilization and decrease the cost of electrocatalysts.[24–26] In this context, single atom catalysts (SACs) have been shown to dramatically reduce the usage of rare and expensive platinum group metals (PGMs) in heterogeneous catalysis, at the same time providing the possibilities for tuning their electrocatalytic properties.[27] SACs are a class of single site catalysts generally composed of reactive dopants atomically isolated in a less reactive metal host. The strong host–dopant interactions that lead to mixing are responsible for the thermal stability of SACs in terms of keeping the dopant site isolated.[28–32] Controlled and large-scale synthesis of stable single atoms and clusters remains a considerable challenge due to the natural tendency of metal atoms to diffuse and agglomerate, resulting in the formation of larger particles. In practical applications, it is required that the single atoms not only have a high activity but also exhibit a satisfactory stability. Moreover, it is also desired to produce single atoms with high density to meet the requirements for practical applications.[33–38] The most adopted synthetic strategies for Pt based SACs include the wet chemistry method, spatial confinement strategy, coordination synthetic strategy, vapor phase deposition and defect

Department of Chemistry and Bar Ilan Institute of Nanotechnology and Advanced Materials (BINA), Bar Ilan University, Ramat Gan, Israel.
E-mail: david.zitoun@biu.ac.il

† Electronic supplementary information (ESI) available. See DOI: https://doi.org/10.1039/d4ya00398e

‡ Equal contribution.

engineering strategy.[39–44] Among them, the wet chemistry method attracted tremendous attention especially for precious metals due to its easy operation without special equipment and potential for large-scale production. All of the abovementioned methods need high energy of activation leading to the formation of clusters or nanoparticles particularly when the loading is greater than 2 wt%. For wet chemistry methods, organometallic complexes have several advantages compared to metal salts and metalorganic precursors. Their low valence state results in low energy activation in the formation of nanoparticles, and their short reaction time can stabilize the formation of kinetically controlled particles. For instance, the core–shell structures of two metals that would alloy under thermodynamic control can be stabilized under kinetic control while reacting two precursors with different decomposition kinetics. For the synthesis of core–shell structures (which is very similar to single atom decoration on a metallic nanoparticle), the core organometallic precursor simply needs to display a lower temperature of decomposition than the shell organometallic one as shown for Fe@Rh,[45] Ru@Pt,[46] or Pd@Ni.[47] Compared to metal salts and metal–organic complexes, a zerovalent organometallic precursor does not undergo a reduction process but the coordination bond with a ligand is activated by a reaction on the ligand (commonly hydrogenation), a mild thermal or photo-activation. The precursors of Pt and Ni are available and have successfully yielded alloyed nanoparticles.[48] Therefore, this approach, by design, yields isolated metallic atoms at very low temperature and can, in principle, be arrested before any diffusion and growth of metallic aggregates. Despite all the promising features of organometallic precursors for single atom synthesis, to the best of our knowledge, there was no report on isolated surface atoms synthesized using an organometallic approach.

In this context, we investigated an organometallic route for achieving high surface coverage of Pt single atoms on Ni nanoparticles supported on carbon. Noteworthily, this synthesis does not need any surfactant, ligand or stabilizer. The overall metal content is set to be 20 wt%, while the Pt : Ni content is set to be 5 : 95 wt% and 10 : 90 wt%. The Ni@Pt SACs synthesized on a carbon support with two different compositions were tested for the hydrogen evolution reaction. Pt SACs on Ni show greater activity for the HER in comparison with conventional Pt/C catalysts.

2. Experimental section

2.1. Materials

$Ni(COD)_2$ (STREM, 98%) and $Pt_2(dba)_3$ (STREM, 98%) were used without further purification. A commercial Pt/C catalyst was purchased from PREMETEK. All chemicals were used as received. Deionized water was distilled using a Milli-Q ultrapure-water purification system. All glassware and Teflon-coated magnetic stirring bars were cleaned with aqua regia, followed by copious rinsing with deionized water before drying in an oven.

2.2. Synthesis of carbon supported Ni with Pt SACs

The carbon supported Ni with Pt SACs were prepared by the simultaneous decomposition of $Ni(COD)_2$ and $Pt(dba)_3$ onto a carbon substrate (Vulcan-XC72). The use of organometallic precursors allows the synthesis under mild conditions of nanoparticles having uniform small size (<5 nm). The resulting SAAs were characterized and electrochemically tested. According to the literature data, deposition of resulting metal NPs onto Vulcan XC-72 has been achieved in the last reaction stages. The significant improvement of the method is deposition of organometallic precursors onto Vulcan-XC72 through a one-pot synthesis. We have developed reaction conditions which make it possible to obtain well dispersed carbon supported Ni@Pt SAAs with two different Pt loadings (5 wt% and 10 wt%, hereafter denoted as Ni@Pt-5 and Ni@Pt-10, respectively). The carbon loading in both cases is maintained to be 80%.

Vulcan-XC72 (0.2 g) was dispersed in 20 ml of dry toluene (anhydrous, 99.9%, Sigma Aldrich) at room temperature for 2 h under a N_2 atmosphere and continuous stirring.

2.2.1. Synthesis of Ni@Pt-10. In a glovebox, 0.680 mmol of $Ni(COD)_2$ and 0.0102 mmol $Pt_2(dba)_3$ were sequentially introduced into 20 ml of the Vulcan-XC72 suspension, one after the other. The stirring continued for 1 hour. The solution was then transferred to a Fisher-Porter tube for the thermal decomposition of organometallic precursors under 1 bar of H_2 atmosphere at 80 °C. The resulting SACs were precipitated by centrifugation (11 000 rpm × 20 min) and washed 3 times with a mixture of ethanol : toluene (1 : 1) (11 000 rpm × 15 min) and then with ethanol (11 000 rpm × 15 min). The SAAs were dried under a vacuum of 3×10^{-3} mbar to remove the residues of organic materials.

2.2.2. Synthesis of Ni@Pt-5. For the synthesis of Ni@Pt-5, the quantities of $Ni(COD)_2$ and $Pt_2(dba)_3$ were adjusted to 0.717 mmol and 0.0051 mmol, respectively.

2.3. Physical characterization

The morphology and elemental compositions of carbon supported Ni@Pt reported in this work were visualized using JEOL JEM-2100 (LaB6) at 200 kV for high resolution imaging. Fourier transform analysis (FFT) of high-resolution images technique was used for structural analysis. High resolution transmission electron microscopy (HRTEM) images together with energy dispersive X-ray spectroscopy (EDS) images were obtained using a JEOL JEM-2100F field emission electron microscope operated at 200 kV. The crystalline phases and crystallinity of the prepared powders of final products were examined using a Rigaku Smartlab XRD in the Bregg–Brentano (theta-two theta) mode. An X-ray generator was operated at 40 kV and 30 mA with Cu-Kα radiation (0.154 nm). X-ray photoelectron spectra (XPS) were recorded using a Thermo Scientific Kα spectrometer with a monochromated Al X-ray source ($h\nu$ = 1486.6 eV; spot size 400 μm). The survey spectra and core-level spectra were recorded with pass energies of 100 and 30 eV, respectively. All spectra were acquired using an electron flood gun to compensate possible positive charge accumulation during the measurements. The obtained spectra were analyzed using S2 CASA XPS software. HAADF-STEM images were taken on a FEI TITAN transmission electron microscope operated at 300 kV. The metal content in the electrocatalysts was determined using a SPECTRA ARCOS ICP-OES Multi view FHX22 instrument. The Pt-L3 edge X-ray

absorption spectra that include extended X-ray absorption fine structure (EXAFS) and X-ray fine near edge structure (XANES) were measured at the SESAME beamline, Jordan.

2.4. Electrochemical measurements

The electrochemical measurements were carried out using a polypropylene cell in a three electrode configuration, with a polished 0.196 cm^2 glassy carbon disk as a working electrode, glassy carbon rod as a counter electrode and Hg/HgO as a reference electrode. The glassy carbon electrode was polished with the α-Al_2O_3 powder of decreasing sizes (1.0–50 nm) and then ultrasonically washed with deionized water and absolute ethanol. Typically, 2 mg of the catalyst mixed with 50 μl of Nafion (5 wt%) solution was dispersed in 950 ml of water–isopropanol solution and sonicated for 1 h to form a homogeneous ink. A micropipette was used to drop 5 μl of the dispersion onto the Glassy carbon surface and then dried at ambient temperature with a rotation rate of 600 rpm. In all cases the total metal loading on the glassy electrode was maintained as 15 μg cm^{-2}. The alkaline aqueous solution was prepared from KOH (Sigma–Aldrich, 99.998%) and ultrapure water. The glassy carbon was mounted on a rotating electrode (Pine instruments) and all the data were collected with a VMP3 potentiostat (Bio-Logic). All gases were used with the highest purity available (99.999%).

3. Results and discussion

3.1. Structural characterization

The carbon supported Ni@Pt nanoparticles were synthesized from organometallic precursors (Fig. 1). The use of organometallic compounds has several advantages when compared to the use of metal salts and metalorganic precursors. Their low valence results in low-energy activation for the formation of nanoparticles. The organometallic complex bis-(cyclooctadiene)nickel(0), $Ni(COD)_2$, undergoes thermal decomposition at 80 °C to yield Ni (0) films and nanocrystals,[49–55] while the organometallic compound bis-(dibenzylideneacetone)-platinum (0), $Pt(dba)_3$, has successfully yielded Pt(0) nanoparticles.[48,56] Syntheses from organometallic compounds can be performed at low temperature or in a short reaction time, which can stabilize the formation of kinetically controlled particles without equilibrium structures. The ICP-OES measurements show the quantitative formation of a 20 wt% metal loading on carbon with a Pt/Ni weight ratio of 95/5 and 90/10 for samples Ni@Pt-5/C and Ni@Pt-10/C, respectively.

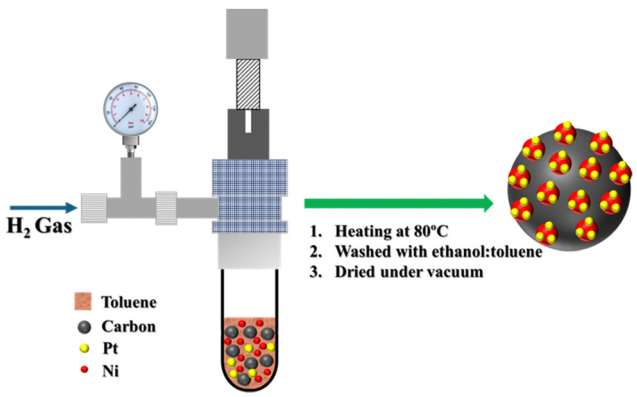

Fig. 1 Schematic representation of the single-step synthesis of Pt SACs on C/Ni from organometallic precursors.

Nanoparticles yielded by the organometallic precursor on the carbon support were analyzed using transmission electron microscopy (TEM) (Fig. 2A, B and Fig. S1 and S3, ESI†). Both the samples Ni@Pt-5/C and Ni@Pt-10/C (10%) show polydispersity (<10%) and the average particle size is found to be 5.8 ± 0.5 nm. The elemental map of Ni@Pt-10/C in Fig. 2C shows homogeneous dispersion of Pt single atoms on Ni nanoparticles. According to the powder X-ray diffraction (PXRD) pattern shown in Fig. 2D, the organometallic approach yields a very disordered phase with very broad and asymmetric peaks. The XRD patterns of pure Ni and Ni@Pt are compared. The characteristic XRD profile of Ni nanoparticles on carbon shows the peaks assigned to the (111), (200) and (220) reflections of face centered cubic (fcc) nickel. The peaks of Ni@Pt SACs with different Pt loadings were located at similar positions to those of Ni nanoparticles. The absence of Pt crystalline peaks in the XRD patterns of Ni@Pt-5/C and Ni@Pt-10/C suggests that there are no apparent Pt particles or agglomerates.

The morphology of Ni@Pt SAAs was characterized by high angle annular diffraction (HAADF) imaging with aberration corrected scanning transmission electron microscopy. The high spatial resolution allowed for the precise determination of size and distribution of the individual metal atoms, thus providing the local structural information regarding the metal atoms on the Ni support. Fig. 3A and Fig. S2 (ESI†) show the HAADF image of Ni@Pt-10/C, which clearly confirms the presence of Pt single atoms (the bright spots) on Ni nanoparticles. The HADDF–STEM-EDS elemental map of Ni@Pt-10/C is shown in Fig. 3B–E. The EDS elemental mapping confirms the uniform distribution of Ni@Pt SACs on carbon.

To investigate the atomic composition and surface oxidation states of metals, we obtained the XPS spectra (Fig. 4). In the XPS spectrum of NiPt-10/C, the Ni 3p characteristic peak appears in the Pt 4f region, this result indicates the simultaneous decomposition of Ni and Pt organometallic precursors resulting in the formation of NiPt single atoms. The Ni 3p characteristic peak intensity decreased by the higher loading of Pt atoms on the Ni nanoparticles in NiPt-10/C than in NiPt-5/C (a low amount of Pt atom loading), suggesting that Pt atoms cover the surface of Ni.[57] In addition, metallic Pt binding energy shifts positively (70.33 eV for NiPt-10/C compared to 70.09 eV for NiPt-5/C), which is due to the formation of Pt surface atoms on Ni (Fig. 4A and Fig. S5D, ESI†). The Ni 2p core level spectrum shows the various oxidized forms of Ni (Ni^{II} – 854.11 eV for NiPt-5/C and 854.52 eV for NiPt-10/C) and Ni^{III} – 856.14 eV for (NiPt-5/C and 856.38 eV for NiPt-10/C) as shown in Fig. 4B and Fig. S4C (ESI†).[58–62] In the case of bare Ni/C without Pt loading on the Ni nanoparticles, we observed Ni(0) and Ni(II) (probably a metallic core with surface oxide) as shown in Fig. S6 (ESI†), which confirms the formation of Ni^0 from the organometallic

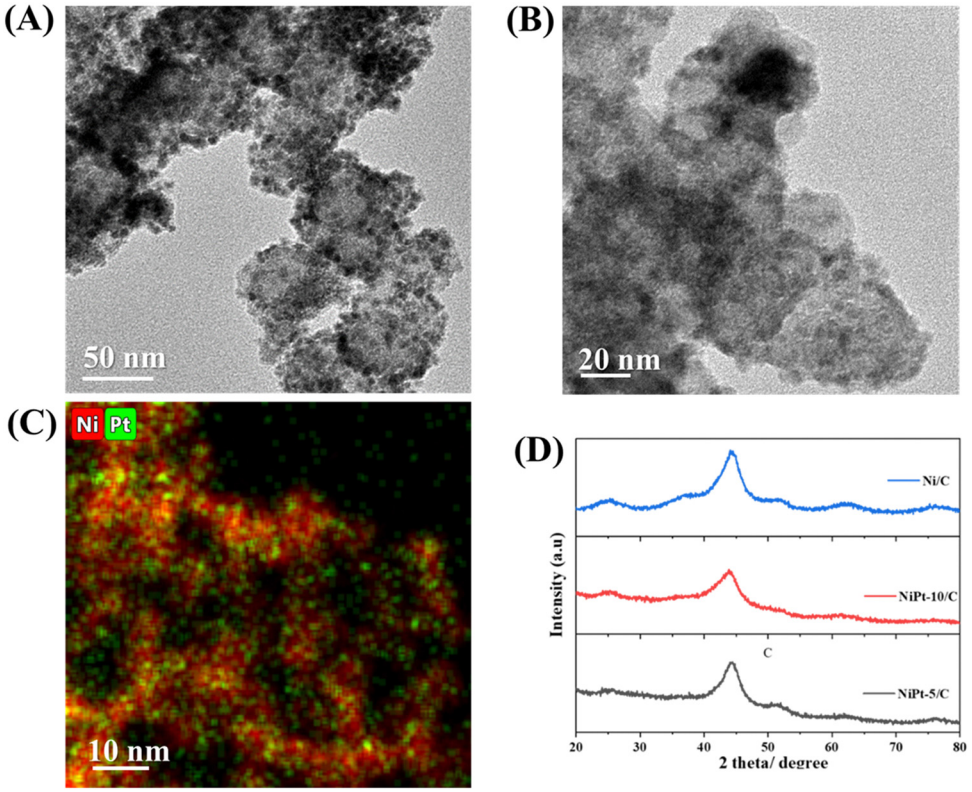

Fig. 2 Microscopy and diffraction analysis, (A) and (B) TEM images of Ni@Pt-10/C with different magnifications. (C) HAADF-STEM elemental map of Ni@Pt-10/C, and (D) XRD patterns of Ni/C, Ni@Pt-10/C and Ni@Pt-5/C.

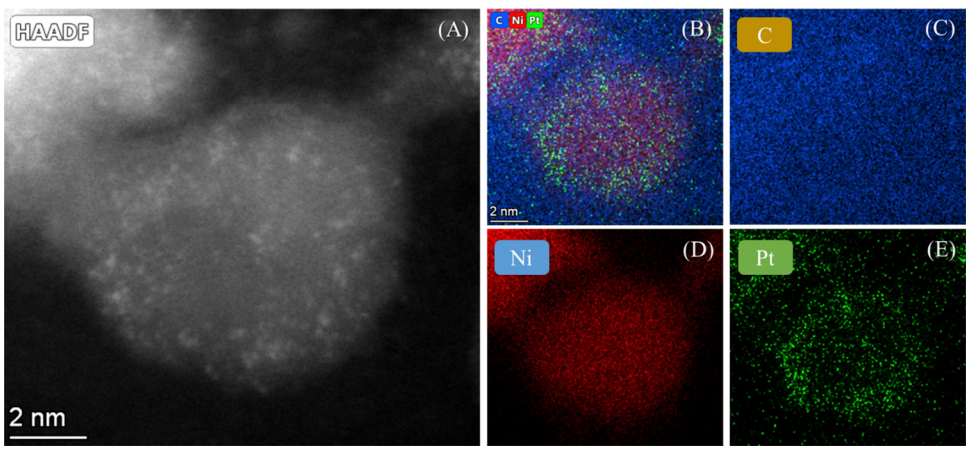

Fig. 3 (A) HAADF image of NiPt-10/C and (B–E) STEM-EDS map of different elements in NiPt-10/C.

precursor without further high temperature heat treatment like that used for other metallic or metalorganic precursors. These XPS findings, together with the TEM and HAADF images, suggest that the formation of NiPt (core) and Pt-incorporated Ni oxide/hydroxide (surface). Other than the Pt 4f and Ni 2p spectra, high resolution C1s and O1s spectra of Ni/C, NiPt-5/C and NiPt-10/C are deconvoluted and are shown in Fig. S4–S6 (ESI†). The precise atomic ratio between Ni and Pt in the NiPt-5/C and NiPt-10C electrocatalysts was determined using ICP-AES, involving complete sample dissolution with 8% HNO_3. The ICP-AES analysis indicates an atomic ratio of Ni : Pt 95 : 5 in NiPt-5/C, while 90 : 10 in NiPt-10/C. These results confirm the quantitative reaction mechanism and the presence of a high density of Pt atoms on the surface of Ni nanoparticles.

Furthermore, the Pt XANES spectrum (Fig. S7A, ESI†) showed a strong white line peak, indicating that Pt is exposed on the surface. The EXAFS spectrum (Fig. S7B, ESI†) showed no apparent peak at 2.57 Å like that of the Pt foil and there is clear

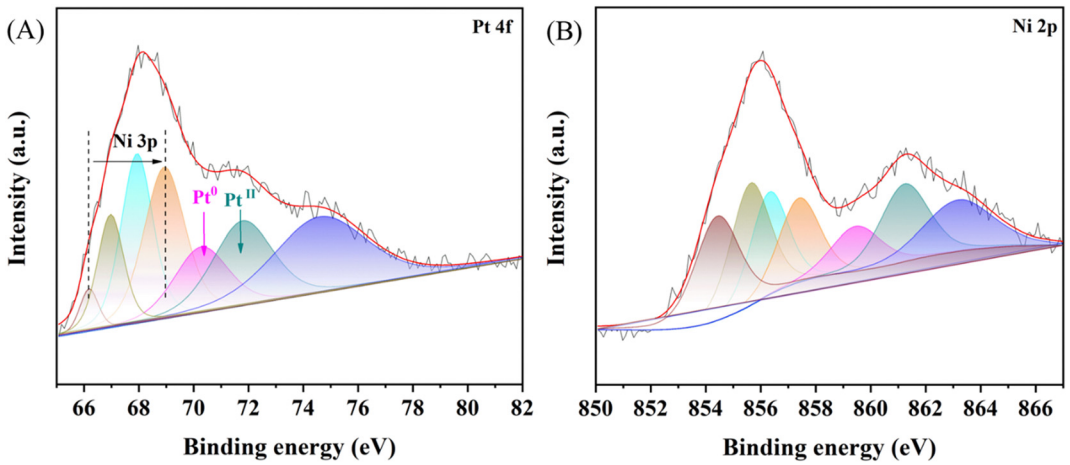

Fig. 4 (A) XPS spectrum of Pt 4f, and (B) Ni 2p for Ni@Pt-10/C.

strong peak at 2.25 Å, suggesting the bond formation of Ni core–Pt surface atoms.

3.2. Electrochemical measurements

The cyclic voltammograms (CVs) of Ni/C and NiPt/C are presented in Fig. 5A. The NiPt SAAs demonstrate superior HER activity compared to Ni/C. Notably, NiPt exhibits reduced Ni oxidation compared to Ni/C and shows a lower onset potential for the oxygen evolution reaction (OER). This behavior suggests that the addition of Pt significantly alters the electronic properties of Ni, which can be effectively tuned by incorporating minimal amounts of Pt, providing a promising strategy to improve water oxidation in alkaline media. The HER performance of NiPt-5/C and NiPt-10/C SAAs was measured in comparison with that of Ni/C and commercial Pt/C (20 wt%) in 0.1 M KOH at room temperature. The Ni nanoparticles on carbon without Pt single atoms exhibited a poor HER

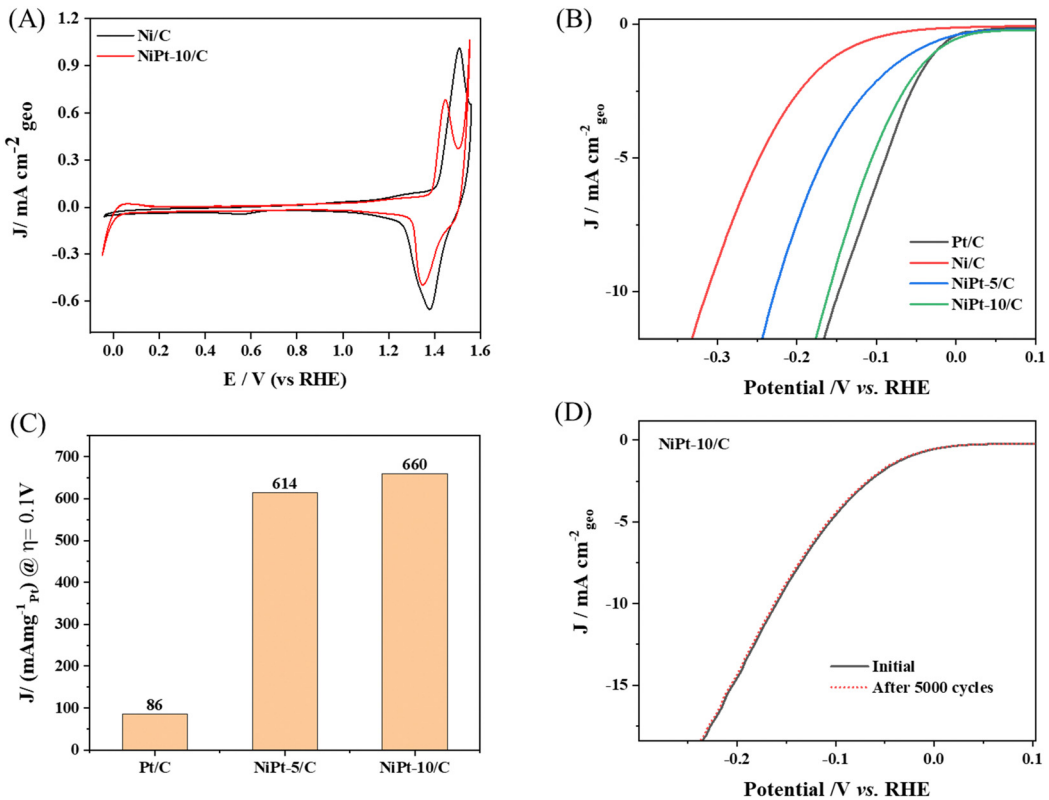

Fig. 5 (A) Comparison of CVs of Ni/C and NiPt-10/C, (B) LSVs for HER activity of Pt/C, Ni/C, NiPt-5/C and NiPt-10/C, and (C) mass activity comparison of different catalysts used in this study. (D) LSVs of NiPt-Pt-10/C before and after 5000 cycles.

performance, which is consistent with the reported literature. The specific activity of each catalyst was calculated from the polarization curves by normalizing the current with the geometric area of the electrode as shown in Fig. 5(B). NiPt-10/C exhibits a more favorable onset potential for the HER compared to standard Pt/C. However, the overpotential required to reach a current density of 10 mA cm^{-2} is 0.159 V for NiPt-10/C and 0.147 V for Pt/C. Although there are fewer Pt active sites available on the NiPt SAAs, alloying Ni with Pt enhances the HER kinetics in alkaline media. This improvement is attributed to the modification of the Pt's electronic structure, which fine-tunes the binding energies of hydroxyl ions (OH*) and hydrogen (H*). The optimized ratio of Pt to Ni shifts the d-band center between two metals, assisting in modulating the adsorption energy of H intermediates on the surface of NiPt SAA. As a result, the onset potential of NiPt-10/C surpasses that of Pt/C.

At higher negative potential, the adsorption of OH^- on the Ni active sites becomes excessively strong, resulting in challenges in OH^- desorption. However, the LSV results indicate that Pt/C outperforms NiPt-10/C, with a difference of just 12 mV. Notably, NiPt-10/C demonstrates a significantly better performance than NiPt-5C (0.228 V), Ni/C (0.314 V) and many other Pt-based electrocatalysts reported for the HER.

Furthermore, normalizing the Pt loading, the HER mass activity of NiPt-10/C at an overpotential of 0.1 V reaches 660 mA mg_{Pt}^{-1}, which is remarkably 8 times greater than that of a commercial Pt/C catalyst. The normalized mass activity of different catalysts is shown in Fig. 5C. These findings suggest that the presence of single Pt atoms significantly enhances the Pt utilization compared to nanoparticle's counterparts, while also offering the advantage of reduced cost. A comparison of the electrocatalytic activity of NiPt-based catalysts with that of other reported catalysts is presented in Table S1 (ESI†). The role of the carbon support is critical in this enhancement. The high-surface-area carbon facilitates optimal dispersion of the Pt single atoms on the Ni nanoparticles, promoting better metal–support interactions and maximizing active site availability. This synergy not only improves catalytic performance but also contributes to the overall stability of the catalyst.

The long-term catalytic stability of NiPt-10/C was measured by cycling the electrocatalyst in the potential window of 0.1 V to −0.25 V 5000 times. Notably, there was no appreciable change in overpotential after the durability test, confirming the stability of Pt single atoms on nickel nanoparticles as shown in Fig. 5D. These results open up a new avenue for the synthesis of stable and active PGM based single atom catalysts on top of metal substrates.

4. Conclusion

In conclusion, NiPt SAA catalysts synthesized *via* a novel one-step organometallic approach on a carbon support demonstrate significant catalytic activity for the HER. The spontaneous segregation of Pt to the surface of Ni at low temperatures allows for precise tuning of the Pt atom density by varying the precursor composition. The precise control over Pt atom dispersion on Ni nanoparticles, combined with a high-surface-area carbon support, optimize the metal–support interaction and increase active site availability, enhancing overall catalytic performance. The NiPt-10/C catalyst exhibits an exceptionally high mass activity of 660 mA mg_{Pt}^{-1}, which is 8 times greater than that of commercial Pt/C, alongside remarkable stability. The remarkable performance of these Pt SACs is attributed to their high density and unique electronic structure on the surface of Ni nanoparticles. Our work provides a promising strategy for designing highly active and stable next-generation catalysts based on PGM single atoms. Future work should focus on optimizing the metal–support interface and refining the alloy structure to further improve both activity and durability.

Data availability

All the data presented in this article are available in the manuscript.

Conflicts of interest

There are no conflicts to declare.

Acknowledgements

The research was partially funded by the Israel Science Foundation and the United-States/Israel Bilateral Science Foundation.

References

1 J. Zhang, C. Liu and B. Zhang, *Small Methods*, 2019, **3**, 1–15.
2 K. Koizumi, K. Nobusada and M. Boero, *Chem. – Eur. J.*, 2017, **23**, 1531–1538.
3 P. A. Østergaard, N. Duic, Y. Noorollahi, H. Mikulcic and S. Kalogirou, *Renewable Energy*, 2020, **146**, 2430–2437.
4 A. Midilli, I. Dincer and M. Ay, *Energy Policy*, 2006, **34**, 3623–3633.
5 A. M. Oliveira, R. R. Beswick and Y. Yan, *Curr. Opin. Chem. Eng.*, 2021, **33**, 100701.
6 P. J. Megia, A. J. Vizcaino, J. A. Calles and A. Carrero, *Energy Fuels*, 2021, **35**, 16403–16415.
7 S. Atilhan, S. Park, M. M. El-Halwagi, M. Atilhan, M. Moore and R. B. Nielsen, *Curr. Opin. Chem. Eng.*, 2021, **31**, 100668.
8 D. J. Jovan and G. Dolanc, *Energies*, 2020, **13**, 6599.
9 Y. F. Wang, C. H. Tsai, W. Y. Chang and Y. M. Kuo, *Int. J. Hydrogen Energy*, 2010, **35**, 135–140.
10 A. D. Selejan, H. Lisei, A. M. Cormos, S. Dragan and C. C. Cormos, *Int. J. Hydrogen Energy*, 2024, **52**, 469–484.
11 Y. Deng, S. Li, L. Appels, R. Dewil, H. Zhang, J. Baeyens and H. Mikulcic, *J. Environ. Manage.*, 2022, **321**, 116019.
12 C. Zhang, B. Chen, D. Mei and X. Liang, *J. Mater. Chem. A*, 2019, **7**, 5475–5481.
13 B. Hüner, N. Demir and M. F. Kaya, *Fuel*, 2023, **331**, 125971.

14 R. Wu, J. Xu, C. L. Zhao, X. Z. Su, X. L. Zhang, Y. R. Zheng, F. Y. Yang, X. S. Zheng, J. F. Zhu, J. Luo, W. X. Li, M. R. Gao and S. H. Yu, *Nat. Commun.*, 2023, **14**, 2306.
15 J. Chen, C. Chen, M. Qin, B. Li, B. Lin, Q. Mao, H. Yang, B. Liu and Y. Wang, *Nat. Commun.*, 2023, **14**, 2306.
16 A. B. Laursen, A. S. Varela, F. Dionigi, H. Fanchiu, C. Miller, O. L. Trinhammer, J. Rossmeisl and S. Dahl, *J. Chem. Educ.*, 2012, **89**, 1595–1599.
17 A. H. Shah, C. Wan, Y. Huang and X. Duan, *J. Phys., Chem. C*, 2023, **127**, 12841–12848.
18 C. Hu, C. Lv, N. Zeng, A. Liu, Y. Liu, L. Hu, P. Li, Y. Yao, J. Cai and T. Tang, *Energy Technol.*, 2023, **11**, 1–37.
19 J. Liu, Z. Wang, D. Zhang, Y. Qin, J. Xiong, J. Lai and L. Wang, *Small*, 2022, **18**, 1–8.
20 H. R. Kwon, H. Park, S. E. Jun, S. Choi and H. W. Jang, *Chem. Commun.*, 2022, **58**, 7874–7889.
21 H. Fei, J. Dong, M. J. Arellano-Jiménez, G. Ye, N. Dong Kim, E. L. G. Samuel, Z. Peng, Z. Zhu, F. Qin, J. Bao, M. J. Yacaman, P. M. Ajayan, D. Chen and J. M. Tour, *Nat. Commun.*, 2015, **6**, 1–8.
22 Y. Pan, X. Wang, H. Lin, Q. Xia, M. Jing, W. Yuan and C. M. Li, *Nanoscale*, 2023, **15**, 14068–14080.
23 Z. Wu, Y. Feng, Z. Qin, X. Han, X. Zheng, Y. Deng and W. Hu, *Small*, 2022, **18**, 1–10.
24 W. H. Lai, L. Zhang, Z. Yan, W. Hua, S. Indris, Y. Lei, H. Liu, Y. X. Wang, Z. Hu, H. K. Liu, S. Chou, G. Wang and S. X. Dou, *Nano Lett.*, 2021, **21**, 7970–7978.
25 Z. Li, T. He, D. Matsumura, S. Miao, A. Wu, L. Liu, G. Wu and P. Chen, *ACS Catal.*, 2017, **7**, 6762–6769.
26 B. Lu, Q. Liu and S. Chen, *ACS Catal.*, 2020, **10**, 7584–7618.
27 Z. K. Han, D. Sarker, R. Ouyang, A. Mazheika, Y. Gao and S. V. Levchenko, *Nat. Commun.*, 2021, **12**, 1–9.
28 R. T. Hannagan, G. Giannakakis, M. Flytzani-Stephanopoulos and E. C. H. Sykes, *Chem. Rev.*, 2020, **120**, 12044–12088.
29 Q. Gao, B. Yao, H. S. Pillai, W. Zang, X. Han, Y. Liu, S.-W. Yu, Z. Yan, B. Min, S. Zhang, H. Zhou, L. Ma, H. Xin, Q. He and H. Zhu, *Nat. Synth.*, 2023, **2**, 624–634.
30 A. S. Rosen, S. Vijay and K. A. Persson, *Chem. Sci.*, 2023, **14**, 1503–1511.
31 S. Guerin and B. E. Hayden, *J. Comb. Chem.*, 2006, **8**, 66–73.
32 S. Yang, Z. Si, G. Li, P. Zhan, C. Liu, L. Lu, B. Han, H. Xie and P. Qin, *Small*, 2023, **19**, 2–9.
33 M. Li, K. Duanmu, C. Wan, T. Cheng, L. Zhang, S. Dai, W. Chen, Z. Zhao, P. Li, H. Fei, Y. Zhu, R. Yu, J. Luo, K. Zang, Z. Lin, M. Ding, J. Huang, H. Sun, J. Guo, X. Pan, W. A. Goddard, P. Sautet, Y. Huang and X. Duan, *Nat. Catal.*, 2019, **2**, 495–503.
34 N. Cheng, S. Stambula, D. Wang, M. N. Banis, J. Liu, A. Riese, B. Xiao, R. Li, T. K. Sham, L. M. Liu, G. A. Botton and X. Sun, *Nat. Commun.*, 2016, **7**, 1–9.
35 X. Tian, J. Luo, H. Nan, H. Zou, R. Chen, T. Shu, X. Li, Y. Li, H. Song, S. Liao and R. R. Adzic, *J. Am. Chem. Soc.*, 2016, **138**, 1575–1583.
36 Q. Wang, B. Zhu, F. Tielens, D. Tichit and H. Guesmi, *Appl. Surf. Sci.*, 2021, **548**, 149217.
37 Y. Peng, Z. Geng, S. Zhao, L. Wang, H. Li, X. Wang, X. Zheng, J. Zhu, Z. Li, R. Si and J. Zeng, *Nano Lett.*, 2018, **18**, 3785–3791.
38 Z. Cao, Q. Chen, J. Zhang, H. Li, Y. Jiang, S. Shen, G. Fu, B. A. Lu, Z. Xie and L. Zheng, *Nat. Commun.*, 2017, **8**, 15131.
39 M. T. Darby, E. C. H. Sykes, A. Michaelides and M. Stamatakis, *Top. Catal.*, 2018, **61**, 428–438.
40 H. L. Skriver and N. M. Rosengaard, *Phys. Rev. B: Condens. Matter Mater. Phys.*, 1992, **46**, 7157–7168.
41 J. Mao, J. Yin, J. Pei, D. Wang and Y. Li, *Nano Today*, 2020, **34**, 100917.
42 Y. Yao, S. Hu, W. Chen, Z. Q. Huang, W. Wei, T. Yao, R. Liu, K. Zang, X. Wang, G. Wu, W. Yuan, T. Yuan, B. Zhu, W. Liu, Z. Li, D. He, Z. Xue, Y. Wang, X. Zheng, J. Dong, C. R. Chang, Y. Chen, X. Hong, J. Luo, S. Wei, W. X. Li, P. Strasser, Y. Wu and Y. Li, *Nat. Catal.*, 2019, **2**, 304–313.
43 L. Nguyen, S. Zhang, L. Wang, Y. Li, H. Yoshida, A. Patlolla, S. Takeda, A. I. Frenkel and F. Tao, *ACS Catal.*, 2016, **6**, 840–850.
44 J. Wan, W. Chen, C. Jia, L. Zheng, J. Dong, X. Zheng, Y. Wang, W. Yan, C. Chen, Q. Peng, D. Wang and Y. Li, *Adv. Mater.*, 2018, **30**, 1–8.
45 D. Ciuculescu, C. Amiens, M. Respaud, A. Falqui, P. Lecante, R. E. Benfield, L. Jiang, K. Fauth and B. Chaudret, *Chem. Mater.*, 2007, **19**, 4624–4626.
46 P. Lara, M. J. Casanove, P. Lecante, P. F. Fazzini, K. Philippot and B. Chaudret, *J. Mater. Chem.*, 2012, **22**, 3578–3584.
47 M. Shviro, S. Polani, R. E. Dunin-Borkowski and D. Zitoun, *Adv. Mater. Interfaces*, 2018, **5**, 1701666.
48 M. A. Domínguez-Crespo, E. Ramírez-Meneses, A. M. Torres-Huerta, V. Garibay-Febles and K. Philippot, *Int. J. Hydrogen Energy*, 2012, **37**, 4798–4811.
49 N. Cordente, M. Respaud, M.-J. Senocq, F. Casanove, C. Amiens and B. Chaudret, *Nano Lett.*, 2001, **1**, 565.
50 M. Shviro and D. Zitoun, *Nanoscale*, 2012, **4**, 762–767.
51 M. Shviro and D. Zitoun, *RSC Adv.*, 2013, **3**, 1380–1387.
52 M. Shviro and D. Zitoun, *RSC Adv.*, 2013, **3**, 1380.
53 A. Paszternák, M. Shviro and D. Zitoun, *J. Nanopart. Res.*, 2014, **16**, 2534.
54 A. Paszternák, M. Shviro, L. Nyikos and D. Zitoun, *J. Nanomater.*, 2014, **2014**, 861056.
55 M. Shviro, A. Paszternák, A. Chelly and D. Zitoun, *J. Nanopart. Res.*, 2013, **15**, 1823.
56 J. Solla-Gullón, E. Lafuente, A. Aldaz, M. T. Martínez and J. M. Feliu, *Electrochim. Acta*, 2007, **52**, 5582–5590.
57 Y. S. Kang, J. Y. Jung, D. Choi, Y. Sohn, S. H. Lee, K. S. Lee, N. D. Kim, P. Kim and S. J. Yoo, *ACS Appl. Mater. Interfaces*, 2020, **12**, 16286–16297.
58 Y. Cong, H. Wang, F. Meng, D. Dou, X. Meng, Q. Zhao, D. Cao and Y. Wang, *J. Solid State Electrochem.*, 2022, **26**, 1381–1388.
59 Y. P. Qiu, Q. Shi, L. L. Zhou, M. H. Chen, C. Chen, P. P. Tang, G. S. Walker and P. Wang, *ACS Appl. Mater. Interfaces*, 2020, **12**, 18617–18624.
60 L. Lin, M. Yuan, Z. Sun, H. Li, C. Nan, G. Sun and S. Ma, *Dalton Trans.*, 2018, **47**, 15131–15140.
61 J. Guo, J. Liu, X. Zhang, X. Guan, M. Zeng, J. Shen, J. Zou, Q. Chen, T. Wang and D. Qian, *J. Mater. Chem. A*, 2022, **10**, 13727–13734.
62 C. Zhang, B. Chen, D. Mei and X. Liang, *J. Mater. Chem. A*, 2019, **7**, 5475–5481.